



Variations in Core Packing of GP2 from Old World Mammarenaviruses in their Post-Fusion Conformations Affect Membrane-Fusion Efficiencies

Anastasiya Shulman, Michael Katz, Hadas Cohen-Dvashi, Harry M. Greenblatt, Yaakov Levy and Ron Diskin

Department of Structural Biology, Weizmann Institute of Science, Rehovot, Israel

Correspondence to Ron Diskin: ron.diskin@weizmann.ac.il.

<https://doi.org/10.1016/j.jmb.2019.04.012>

Edited by M.F. Summers

Abstract

Lassa virus (LASV) is a notorious human pathogen in West Africa. Its class I trimeric spike complex displays a distinct architecture, and its cell entry mechanism involves unique attributes not shared by other related viruses. We determined the crystal structure of the GP2 fusion glycoprotein from the spike complex of LASV (GP2_{LASV}) in its post-fusion conformation. GP2_{LASV} adopts a canonical helical bundle configuration similarly to other viruses in its family. The core packing of GP2_{LASV}, however, is more organized compared to GP2 from other viruses reducing the formation of internal hydrophobic cavities. We demonstrate a link between the formation of such unfavorable hydrophobic cavities and the efficiencies of membrane fusion and cell entry. Our study suggests that LASV has evolved a more efficient membrane fusogen compared to other viruses from its family by optimizing the post-fusion configuration of its GP2 module.

© 2019 Elsevier Ltd. All rights reserved.

Introduction

The *Arenaviridae* family of viruses hosts many viral species [1,2], of which some can infect humans and cause severe diseases [3–6]. Lassa virus (LASV), which resides in rodents from the *Mastomys* genus and is endemic to West Africa [2], is the most prevalent mammalian-born hemorrhagic fever Arenavirus (mammarenavirus) [7]. For entering cells, mammarenaviruses utilize trimeric class I glycoprotein spike complexes on their membrane envelopes for attaching to their cellular receptors as well as to facilitate membrane fusion of the virus with its host [8–12]. These spike complexes are translated as glycoprotein precursors (GPCs) that are first cleaved by cellular signal peptidase and later by subtilisin kexin isozyme-1/site-1 protease to give a stable signal peptide as well as glycoproteins 1 and 2 (GP1 and GP2) that make together the functional spikes, which ultimately consist of three fully processed GPCs [13–16]. The GP1 modules mediate attachment to the cellular receptors [17,18] and the membrane-encored GP2 modules mediate membrane fusion at a late endosomal compartment to allow viral invasion into the cytoplasm [10,19,20].

Membrane fusion by class I viral fusogens is thought to follow a specific set of structural rearrangements. Upon triggering, the native GP2 first extends to allow special hydrophobic loops, termed the fusion loops, to penetrate the target membrane and then these short-lived extended intermediates collapse to a characteristic helical bundle configuration that forces the viral and the target membranes into proximity, which drives fusion (reviewed in Ref. [19]).

It has been increasingly appreciated in recent years that mammarenaviruses utilize multiple cell entry strategies that fundamentally differ from one another. While most mammarenaviruses that are endemic to South and North Americas (New World mammarenaviruses) utilize transferrin receptor-1 as a cell-entry receptor [18,21–26], the Africa-endemic Old World mammarenaviruses mostly utilize α -dystroglycan [27–30] and in some conditions other alternative receptors [31,32]. The recently emerged Lujo mammarenavirus utilizes neuropilin-2 for cell entry [17,33]. Hence, there is substantial diversity in receptor usage among viruses of this family. Moreover, during entry, LASV switches from α -dystroglycan to lysosomal-associated membrane protein 1 (LAMP1) [34] that promotes the triggering

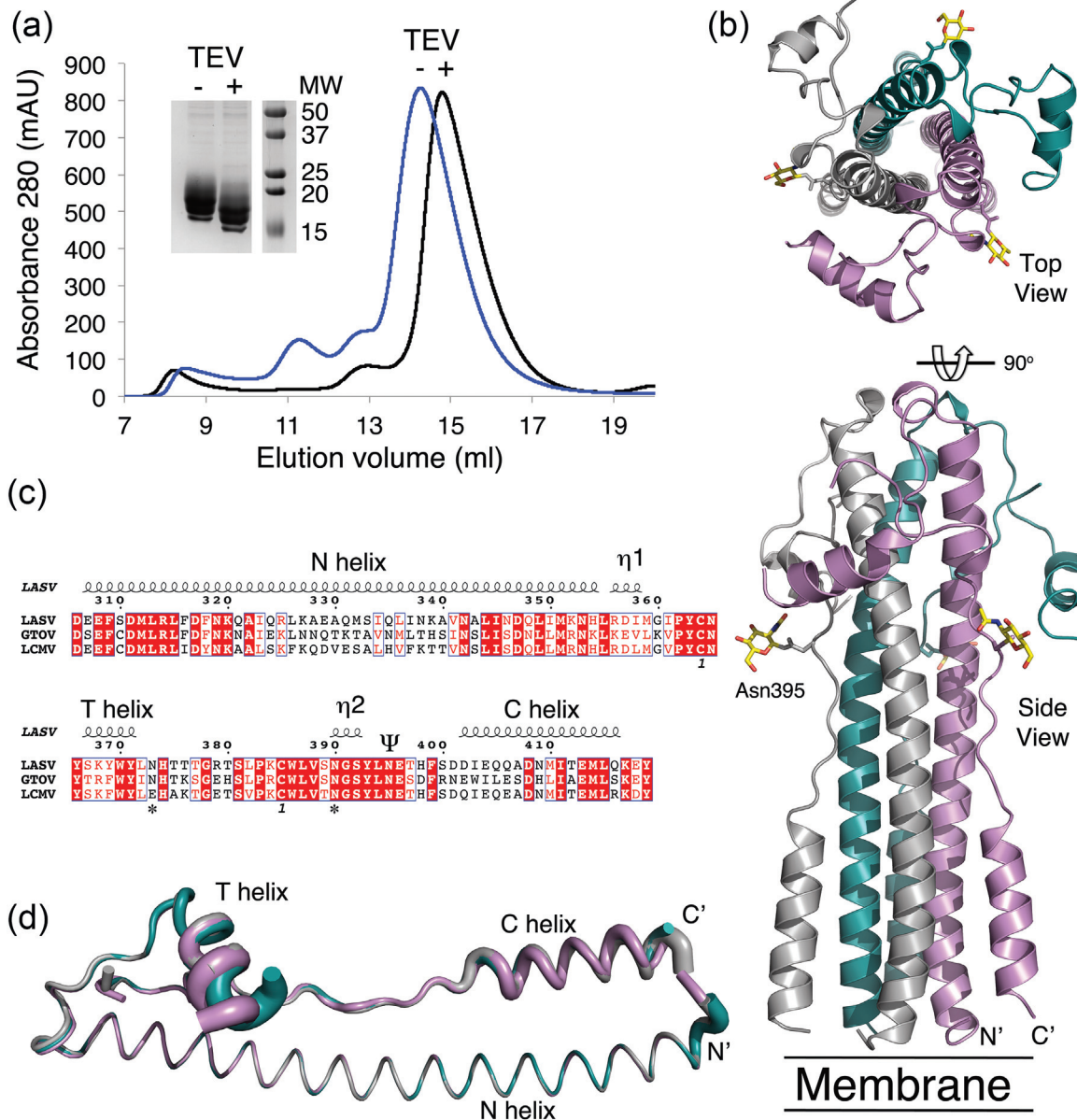


Fig. 1. Determining the crystal structure of GP2_{LASV}. (a) Chromatogram showing the elution profile of GP2_{LASV} from size exclusion column before (blue) and after (black) cleavage of the His6 tag. An inset shows SDS-PAGE analysis of the GP2_{LASV} before and after cleavage using Coomassie staining. The presence of several glycoforms is evident. (b) Ribbon diagram of the trimeric GP2_{LASV} in top and side views (upper and lower images, respectively). Each of the three chains that compose the trimeric structure is shown in a different color. The first *N*-acetylglucosamine of a glycan attached to Asn395 is shown as sticks. The termini of a representative chain are marked as well as the expected location of the lipid membrane for context. (c) Multiple-sequence alignment of GP2 subunits from Lassa (LASV), Lymphocytic choriomeningitis virus (LCMV) and Guanarito (GTOV) mammarenaviruses showing the organization of the secondary structure elements as observed in the crystal structure. The numbering of the amino acids is based on the sequence of Lassa glycoprotein. Fully conserved residues are highlighted with a red background, and partially conserved residues are shown in red. The location of the disulfide bridge is designated with the figure "1." The symbol " Ψ " marks the observed glycosylated site. This graphical representation was generated by ESPript [44] (<http://esprict.ibcp.fr>). (d) Superimposition of the three chains of GP2_{LASV} that were modeled in the crystallographic asymmetric unit and make one complete trimer. The chains are represented as tubes with a width that is proportional to their *B*-factor.

Table 1. Data collection and refinement statistics

| PDB ID | 5OMI |
|--|---|
| Data collection | |
| Wavelength (Å) | 0.9762 |
| Space group | $C222_1$ |
| Cell dimensions (Å, °) | $a = 58.32, b = 103.43, c = 171.55, \alpha = \beta = \gamma = 90$ |
| Resolution (Å) | 49.52–2.56 (2.65–2.56) ^a |
| R_{meas} (%) | 7.5 (171.8) ^a |
| R_{pim} (%) | 2.9 (66.1) ^a |
| $CC_{1/2}$ | 99.7 (66.2) ^a |
| I/σ | 13.8 (1.1) ^a |
| Completeness (%) | 99.9 (100.0) ^a |
| Multiplicity | 6.6 |
| Wilson B -factor (Å ²) | 69.8 |
| Total reflections | 112,332 |
| Unique reflections | 17,135 |
| Refinement | |
| Resolution (Å) | 49.52–2.56 |
| No. of reflections | 17,098 |
| $R_{\text{work}}/R_{\text{free}}$ (%) ^b | 23.7/28.7 |
| No. of atoms | |
| Protein | 2665 |
| Ligand/ion | 45 |
| Water | 4 |
| TLS groups | 14 |
| Model quality | |
| MolProbity (score, %-ile) | 1.58, 99th |
| B factors | |
| Protein, ligand/ion, water | 114, 162, 75 |
| Ramachandran | |
| Favored, allowed, outliers (%) | 99.0, 1.0, 0.0 |
| Rotamers | |
| Favored, Poor (%) | 96.6, 0.3 |
| Root mean square deviations | |
| Bond length (Å) | 0.006 |
| Bond angles (°) | 0.935 |

^a Values in parentheses are for the highest-resolution shell.

^b Test set size for calculating R_{free} was 10% (1713 reflections).

of the spike complex and facilitates efficient cell entry [35], a mechanism that is not shared by other Old World mammarenaviruses [36]. The different cell entry mechanisms determine the efficiency of cell entry and may thus ultimately affect the virulence of these viruses.

Since LASV is a critical human pathogen, substantial effort is devoted for studying its spike complex and its cell entry process at the molecular level. We previously determined the structure of its GP1 receptor-binding module in a primed conformation and identified regions that are important for binding to LAMP1 [37]. The Ollmann–Saphire laboratory recently deciphered the native conformation of the trimeric ectodomain portion from the spike complex of LASV (GPC_{LASV}) [38]. This structure revealed the native conformations of both the GP1

and GP2 modules. The complete GPC_{LASV} in the context of the membrane was also studied at low resolution using electron microscopy [39]. This study revealed that the trimeric spike undergoes pH-induced conformation changes that likely prepare it to bind LAMP1 [39], prior to triggering of membrane fusion. This study further provided a low-resolution reconstruction of the LASV GP2 portion (GP2_{LASV}) membrane-embedded stem in the post-fusion conformation after the dissociation of GP1 [39]. Surprisingly, this density differed from the expected canonical post-fusion helical bundle that characterize class I fusogens [39]. Post-fusion structures of GP2 modules of mammarenaviruses were previously determined: The structures of GP2 from the Old World lymphocytic choriomeningitis mammarenavirus (GP2_{LCMV}) [40] and subsequently of GP2 from the New World guanarito mammarenavirus (GP2_{GTOV}) [41] were determined using x-ray crystallography, revealing canonical six-helical bundles. It was thus highly intriguing whether GP2_{LASV} also adopts a six-helical bundle configuration in its post-fusion state, and whether such putative configuration differs from the GP2 modules of other mammarenaviruses. In this study, we present the post-fusion structure of GP2_{LASV} that was determined using x-ray crystallography. We found that it nevertheless adopts a six-helical bundle configuration. We further identified critical differences in the packing of its core compared to other GP2 modules of mammarenaviruses, which influence its fusogenic activity. These differences provide a partial explanation for the virulence of LASV.

Results

GP2_{LASV} adopts a canonical helical bundle fold in its post-fusion conformation

As part of an effort to better understand the differences in cell entry mechanisms of LASV compared to other mammarenaviruses, we determined the structure of its GP2 fusogen in a post-fusion conformation. For that, we constructed a truncated version of GP2_{LASV} spanning residues 306–421, which is lacking the N-terminal hydrophobic fusion peptides as well as the transmembrane and cytoplasmic regions, following the same general strategy that was previously used to solve the structures of GP2_{LCMV} [40] as well as of GP2_{GTOV} [41]. We used a 6xHis affinity tag followed by a TEV (tobacco etch virus) cleavage site at the N' terminus of the protein to facilitate affinity purification. We further introduced a Cys310 to serine mutation to avoid having an unpaired cysteine residue after eliminating its partner disulfide bond cysteine at the N' terminus of the protein. This construct readily

expressed using insect cells and yielded a well-defined peak using size exclusion chromatography (Fig. 1a). The elution volume suggested a molecular weight of about 40 kDa, implying that GP2_{LASV} exists as a trimer in solution (Fig. 1a). Subsequently, the 6xHis affinity tag was removed using enzymatic cleavage with TEV for making the GP2_{LASV} suitable for crystallization (Fig. 1a).

Using vapor diffusion in sitting drops, we obtained GP2_{LASV} crystals in various conditions but most crystals diffracted poorly. After substantial screening efforts, we were able to record a complete x-ray diffraction data set at 2.6-Å resolution (Table 1). Using the structure of GP2_{LCMV} (PDB ID: 3MKO) as a search model, we found a molecular replacement solution for GP2_{LASV}. The final model consists of three GP2_{LASV} protomers that closely interact with each other, forming a canonical six-helical bundle (Fig. 1b). Electron density allowed modeling of residues 304–418, 304–417, and 303–416 for the “A,” “B,” and “C” protomers, respectively (including 2–

3 non-native residues of the linker used at the N' termini). In addition, electron density was poor for residues 375–382, 378–383, and 379–382 of the “A,” “B,” and “C” protomers, respectively, and hence, these residues were not modeled. We further modeled *N*-acetylglucosamine residues attached to Asn395 located in a coil preceding the C' terminal helix (Fig. 1b, c). Superimposing the three chains that make the complete trimeric complex reveal that they adopt nearly identical structures with slight variations near the T helix, which is the most flexible part of the structure (Fig. 1d).

The orientation of C helices vary between GP2 domains of different mammarenaviruses

The sequences of the GP2 modules from various mammarenaviruses are relatively conserved (Fig. 1c); for the ectodomain portion that we crystallized, GP2_{LASV} displays 68% and 52% sequence identity compared with GP2_{LCMV} and GP2_{GTOV}, respectively. Likewise, superimposing a single protomer of GP2_{LASV} with the protomers from GP2_{LCMV} [40] and GP2_{GTOV} [41] reveals that they share a similar overall structure (Fig. 2a). Superimposing GP2_{LASV} with GP2_{LCMV} and GP2_{GTOV} provides RMSDs of 1.95 Å (65 Cα atoms) and 1.14 Å (63 Cα atoms), respectively. Some deviations in conformation are apparent at the T helices as well as in the orientations of the C helices (Fig. 2a). A closer look at the C helices reveals that these changes in orientations alter the way they interact with the N terminal regions of GP2 (Fig. 2b). In GP2_{LASV}, the C helices adopt an orientation that allows them to interact closely with the N helices of adjacent

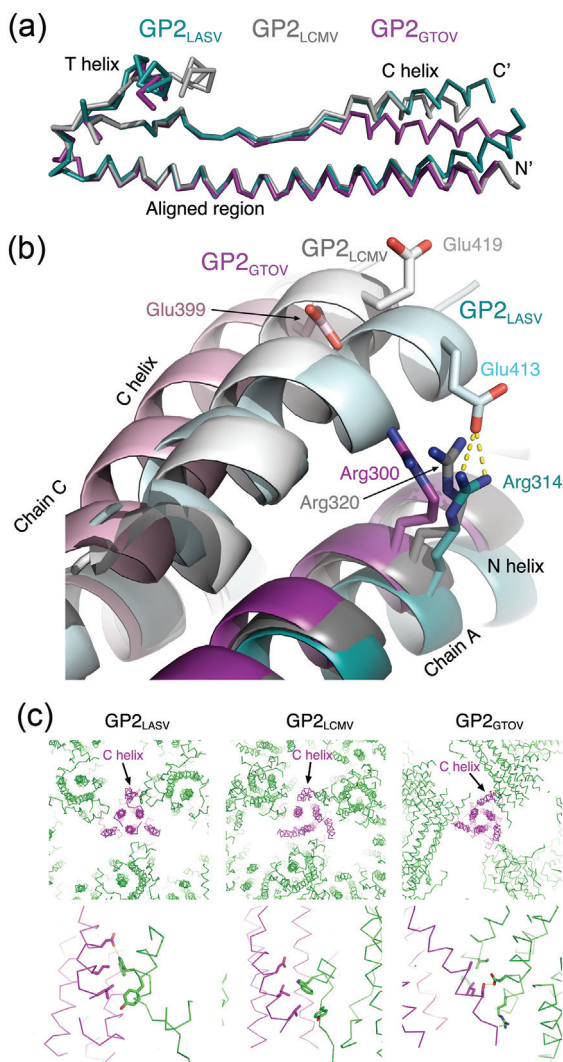


Fig. 2. Comparison of the available GP2 structures from mammarenaviruses in a post-fusion conformation. (a) Superimposition of a representative protomer from GP2_{LASV}, GP2_{LCMV}, and GP2_{GTOV} colored in marine-blue, gray, and magenta, respectively, and rendered as Ca traces. Structural alignment was calculated based on the conserved N helix. (b) Packing of the C helices against the central N helices-coiled coil. Superimposition of the various GP2 structures rendered as ribbons using the same color codes as in “A” showing the relative orientation of the C helices. The C helix from one protomer of the trimer (designated “chain C” and highlighted using bright colors) is interacting with the N helix of an adjacent protomer (designated “chain A” and highlighted in dark colors). A salt bridge that is formed in GP2_{LASV} is shown using dashed yellow lines. (c) Crystal packing of GP2_{LASV}, GP2_{LCMV}, and GP2_{GTOV}. The upper row shows a panel of the different GP2 trimers (magenta) oriented with their trimeric axes perpendicular to the image plane. The crystallographic neighbors are colored green, and one C helix for each trimer is labeled. The lower row shows close-up views of the C helices and their interactions with the nearby crystallographic neighbors. Side chains of residues that participate in forming crystal contacts are represented with sticks.

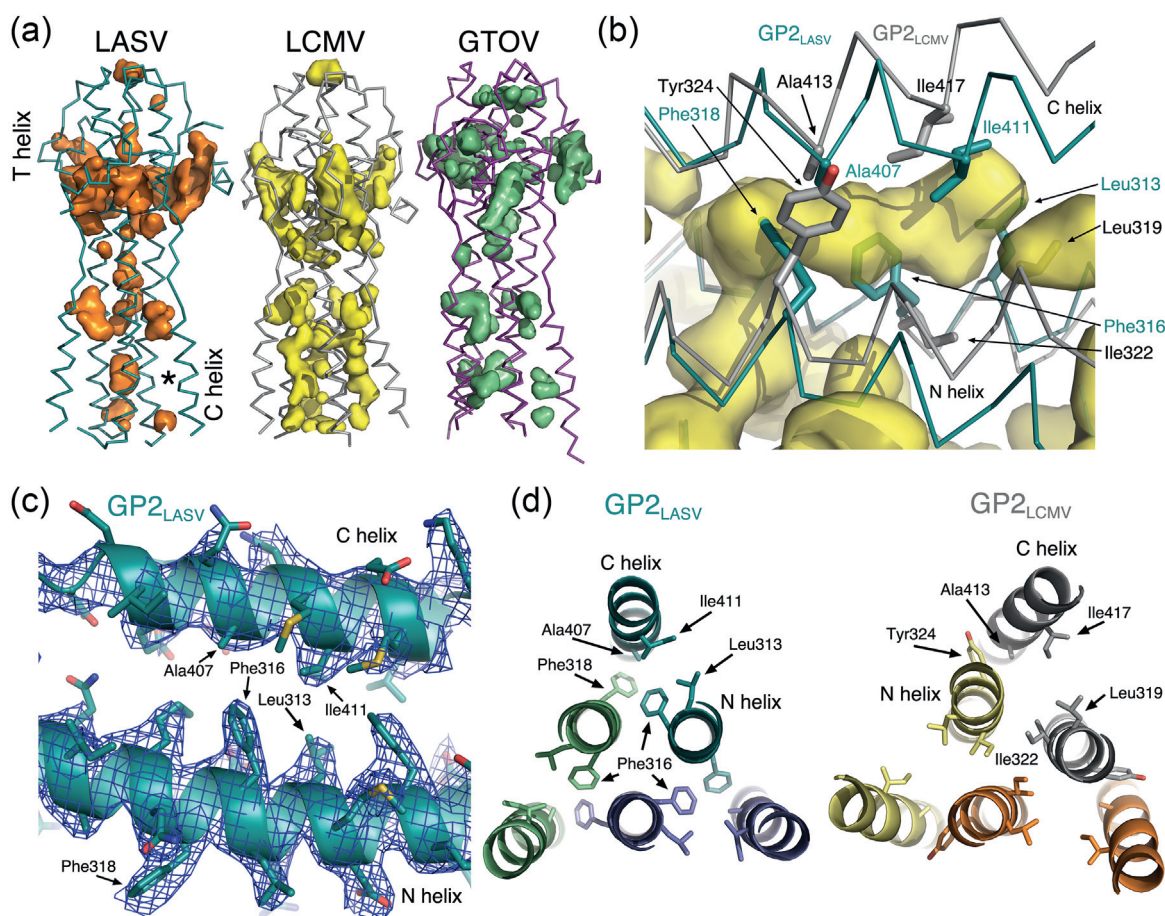


Fig. 3. The C helices of GP2_{LASV} pack tighter compared with other GP2s. (a) Inner cavities at a five solvent detection radii are shown using a surface representation in the structures of GP2_{LASV}, GP2_{LCMV}, and GP2_{GTOV} colored orange, yellow, and green, respectively. The interaction region of a C helix of GP2_{LASV} that is devoid of cavities compared to GP2_{LCMV} is marked with an asterisk. (b) A detailed comparison of the C helices packing in GP2_{LASV} and GP2_{LCMV}. The side-chains of the nearby residues that flank the cavity in the case of GP2_{LCMV}, and occupy the same space of the cavity in the case of GP2_{LASV} are shown as sticks and labeled. (c) $2F_o - F_c$ electron density map at $\sigma = 1$ is shown as a blue mesh. The residues that make the hydrophobic core in GP2_{LASV} are labeled in the figure. (d) Views of the hydrophobic cores from the membrane side along the trimeric axes. GP2_{LASV} is shown on the left-hand side and GP2_{LCMV} is shown on the right-hand side.

protomers. This orientation facilitates the formation of a salt-bridge between Glu413 on the C helices and Arg314 at the N helices (Fig. 2b). Although both GP2_{LCMV} and GP2_{GTOV} have equivalent glutamate residues (Glu419 and Glu399, respectively) and arginine residues (Arg320 and Arg300, respectively), they are too far from each other in both structures to interact (Fig. 2b). Rotameric rearrangement of these residues cannot bring their charged head-groups close enough to form salt bridges as seen in GP2_{LASV}. Instead, the C helices of GP2_{LCMV} and GP2_{GTOV} are closer to the N helices within the same protomers, leading to altered geometry of the membrane-proximal region of these GP2s. Observing the crystallographic packing of the GP2s reveals that both GP2_{LASV} and GP2_{LCMV} adopt a similar head-to-tail packing with very similar contacts

formed by their C helices and the nearby head residues (Fig. 2c). GP2_{GTOV}, on the other hand, is packed differently in the crystal, causing its C helices to make distinct contacts with the crystallographic neighbors (Fig. 2c). Hence, while the unique crystallographic interactions of GP2_{GTOV} may contribute to its altered C helices' conformation, the differences between the C helices of GP2_{LASV} and GP2_{LCMV} likely reflect *bona fide* variations of the proteins.

The C helix of GP2_{LASV} forms a tightly packed hydrophobic core

The diverse orientations of the C helices in the various GP2 modules may potentially result from differences in packing against the N helices. As a

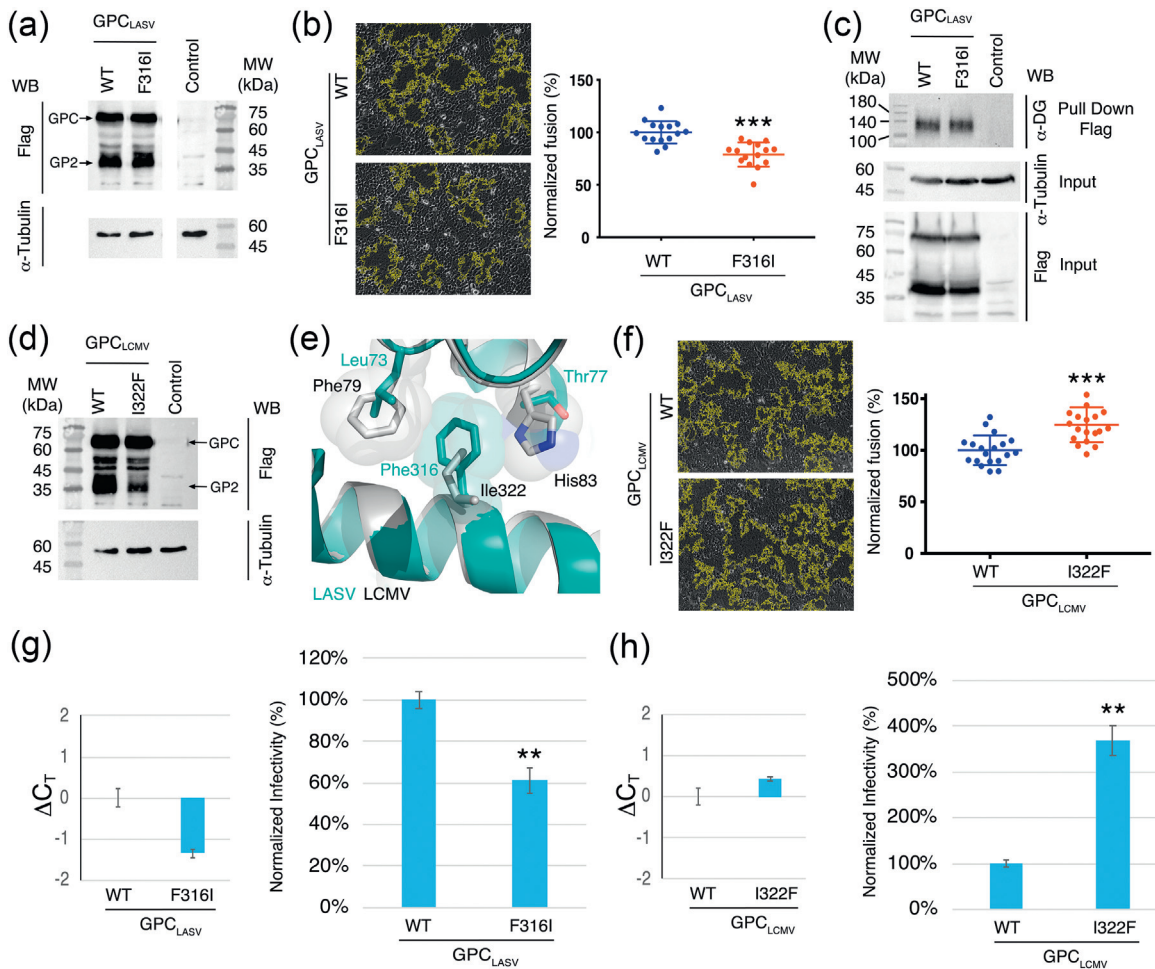


Fig. 4. Packing of the C helix affects membrane fusion efficiency. (a) Expression and processing profiles of GPC_{LASV} compared to GPC_{LASV}-F316I mutant. Western blot analyses show Flag-GPC constructs that were transiently transfected into HEK293 cells. Unprocessed GPCs as well as the GP2 portion after cleavage are indicated with black arrows. Detecting α -tubulin was used as a loading control. This image is a representative one out of two independent repeats. (b) Syncytia formation assay at pH 4.5. Representative raw images from the fusion assay are shown on the left. Membrane fusion activity of GPC_{LASV} (blue, defined as 100%) was compared to the activity of GPC_{LASV}-F316I mutant (red). Each dot represents a single repeat. The difference in activity is statistically significant ($p < 0.001$, two-sided Student's t -test). (c) Pull-down assay of α -dystroglycan (α -DG). The ability of GPC_{LASV} to pull down α -DG was compared to the ability of GPC_{LASV}-F316I mutant. Western blot analysis using anti-Flag shows the GPC input. Levels of α -Tubulin are shown as a loading control of cells extract. Pulled-down levels of α -DG were visualized using an anti- α -DG antibody. This is a representative experiment from two independent repeats. (d) Expression and processing profiles of GPC_{LCMV} compared to GPC_{LCMV}-I322F mutant. Western blot analyses show Flag-GPC constructs that were transiently transfected into HEK293 cells. Unprocessed GPCs as well as the GP2 portion after cleavage are indicated with black arrows. Detecting α -tubulin was used as a loading control. This image is a representative one out of two independent repeats. (e) The vicinity of Ile322 of GPC_{LCMV} in the pre-fusion native structure (PDB ID: 5INE) compared to the pre-fusion structure of GPC_{LASV} (PDB ID: 5VK2). GPC_{LCMV} and GPC_{LASV} are shown as gray and marine-blue ribbons, respectively. Ile322 of GPC_{LCMV} and the corresponding Phe316 of GPC_{LASV} are shown as sticks as well as the nearby residues as indicated. Semi-transparent spheres indicate Van der Waals radii of selected residues. (f) Syncytia formation assay at pH 4.0. Representative raw images from the fusion assay are shown on the left. Membrane fusion activity of GPC_{LCMV} (blue, defined as 100%) was compared to the activity of GPC_{LCMV}-I322F mutant (red). Each dot represents a single repeat. The difference in activity is statistically significant ($p < 0.001$, two-sided Student's t -test). (g and h) The effect of core mutations on spike-mediated cell entry. Normalized infectivity of pseudo-viruses bearing GPC_{LASV} or GPC_{LASV}-F316I (g) and GPC_{LCMV} or GPC_{LCMV}-I322F (h), as measured by the luciferase reporter gene. RT-qPCR was used to quantify the differences in the amounts of pseudotyped viruses, and ΔC_T values are shown. Infectivity levels were calculated from three independent experiments, each consists of multiple technical repeats. The differences are statistically significant (** $p < 0.01$, two-sided Student's t -test).

measure for the packing quality, we examined the internal cavities in the GP2 modules and found intriguing differences (Fig. 3a). We first noticed that all of the GP2 modules have an elaborate set of internal cavities near the T helices, indicating poor packing in these regions. This observation helps to explain the relative excessive motion of the T helices as indicated by their relative higher B factors (Fig. 1d). The packing near the C helices, on the other hand, vary in quality, as there are almost no internal cavities in GP2_{LASV}, while some are visible in GP2_{GTOV}, and more extensive set of cavities exist in GP2_{LCMV} (Fig. 3a). To better understand the source for these differences, we examined the different residues that mediate the packing of the C helices in GP2_{LASV} and GP2_{LCMV} (Fig. 3b). Examining the electron density map in this region indicates sufficient quality for unambiguous assignment of rotamers for the key residues that make the hydrophobic core (Fig. 3c). Since GP2_{GTOV} was determined at a modest resolution of 4.1 Å [41] in which assigning correct rotamers is challenging, and its crystal packing significantly differs from that of GP2_{LASV} or GP2_{LCMV} (Fig. 2c), we decided to omit it from this analysis. There are two major differences between GP2_{LASV} and GP2_{LCMV}: in GP2_{LASV}, two phenylalanine residues (Phe318 from one N helix and Phe316 from an adjacent N helix) make hydrophobic interactions with Ala407 and Ile411 from the C helix (Fig. 3b). In GP2_{LCMV}, on the other hand, Tyr324 that replaces Phe318 is pointing away from the core. Also, Ile322 replaces Phe316 of GP2_{LASV} (Fig. 3b) and is pointing toward the symmetry axis of the GP2 trimer, making mutual self-interactions with isoleucine from adjacent protomers (Fig. 3d). These two changes together with the relative movement of the C helix in respect to the N helices (Fig. 2a) reduce the extent of interactions of the C helix with the N helices and account for the formation of the large cavities in GP2_{LCMV} (Fig. 3a).

The packing of the C helices influence the fusogenic activity of GP2

For membrane fusion, the GP2 fusogen undergoes an elaborated series of conformational changes from its native pre-fusion conformation [19]. First, it adopts an extended intermediate form, in which it anchors its fusion peptide into the target membrane, and then it collapses to form the characteristic post-fusion hairpin conformation while bringing the viral and the target membranes to close vicinity. When the membranes are close enough, the two outer leaflets of the membranes merge to form the hemifusion intermediate, followed by complete fusion and pore formation [19]. Only upon pore formation, the GP2 can fully achieve its post-fusion conformation. The formation of the initial pore does not guarantee fusion as this is a reversible

process, and expansion of the pore is the most energy-demanding step in the fusion process (reviewed by Chernomordik and Kozlov [42]). Given the close proximity to the N' terminal fusion peptide and to the C' terminal trans-membrane domain, the packing quality of the C helices may be important for progressing from the hemifusion intermediate to form the initial pore, as well as to stabilize the pore to allow expansion.

To test a possible influence of the packing of the C helices on fusion, we swapped Phe316 of GPC_{LASV} with isoleucine to generate a variant that would be more similar to GPC_{LCMV}, presumably reducing the extent of hydrophobic interactions between the N and C helices by introducing a cavity in the post-fusion conformation. We first verified that this variant efficiently expresses and is processed similarly to the GPC_{LASV}-WT by following a C' terminal Flag-tag versions of these proteins (Fig. 4a). We then tested the efficiency of GPC_{LASV}-F316I to induce syncytia formation in HEK293 cells that ectopically express it, following exposure to low pH (Fig. 4b). Interestingly, although GPC_{LASV}-F316I induces syncytia formation, it is less efficient than GPC_{LASV}-WT. Potentially, this reduction in fusogenic activity may result from reduced binding to the α -DG cellular receptor. We therefore tested the ability of GPC_{LASV}-F316I to pull down α -DG and found it to be similar to GPC_{LASV}-WT (Fig. 4c). We next performed a reciprocal experiment in GPC_{LCMV} to test a potential effect of augmenting the interaction between the N and C helices by reducing the core cavities on membrane fusion activity. We mutated Ile322 of GPC_{LCMV} to phenylalanine and tested its expression and processing following C' Flag-tag variants (Fig. 4d). Although the expression levels of GPC_{LCMV}-I322F were similar to the expression levels of GPC_{LCMV}-WT, as can be judged by the levels of the unprocessed GPC (Fig. 4d), the levels of the cleaved GP2 portion were lower compared with the WT (Fig. 4d). The reduced amount of processed GPC indicates that the I322F mutation affects the native pre-fusion structure of GPC_{LCMV}. Looking at the structure of the native GPC_{LCMV} (PDB ID: 5INE) [43] and comparing it to the structure of the native GPC_{LASV} (PDB ID: 5VK2) [38] reveals that I322F mutation in GPC_{LCMV} cannot be fully accommodated due to steric interference with the nearby Phe79 and His83 (Fig. 4e). Such steric constraints do not exist in GPC_{LASV} since both Phe79 and His83 are replaced with smaller Leu73 and Thr77, respectively (Fig. 4e). Nevertheless, despite reduced levels of processed GPC_{LCMV}-I322F, it exhibits significantly augmented membrane fusion activity compared to GPC_{LCMV}-WT (Fig. 4f). Finally, we tested if these mutations also affect cell entry of MLV-based pseudotyped viruses that bear the relevant GPCs. To account for the variations in the expression levels of the mutate GPC_{LCMV} versus GPC_{LCMV}-WT, we

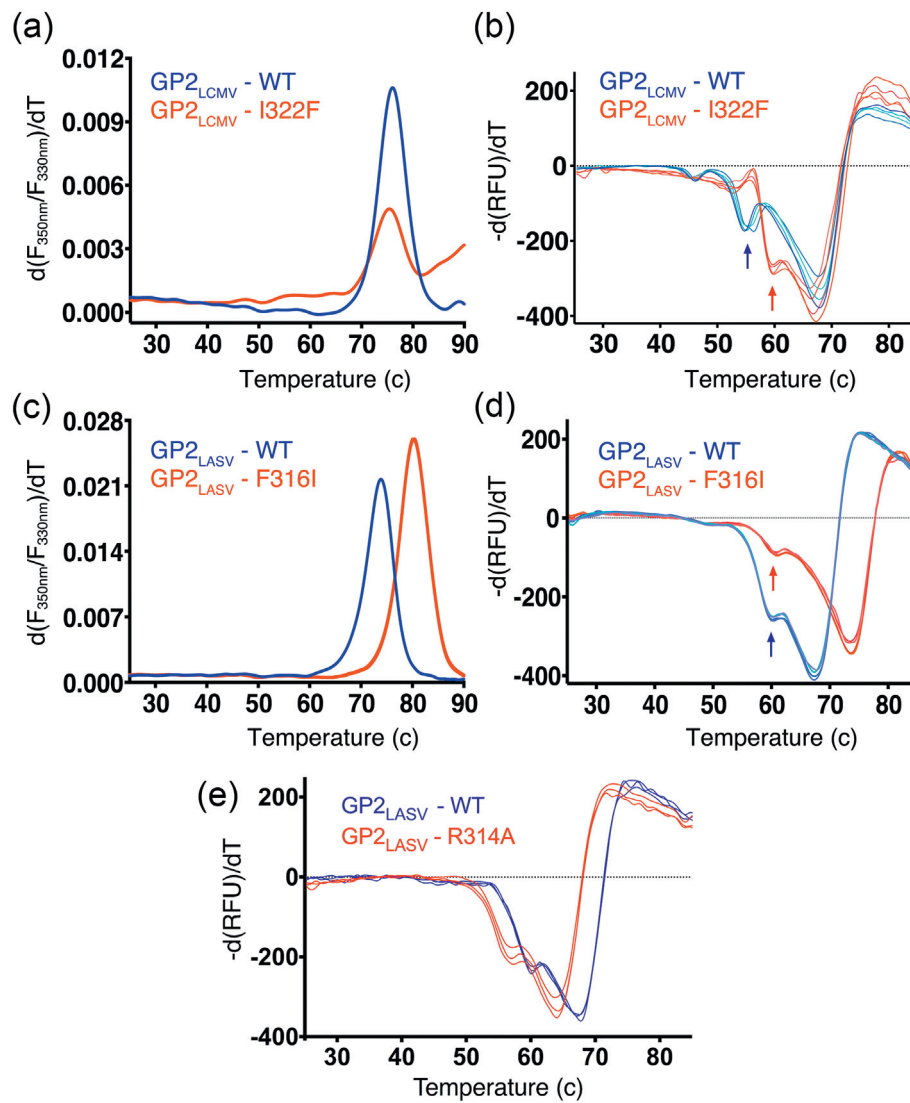


Fig. 5. Modulations of the thermal stability of GP2 in the post-fusion conformation by core packing mutations. (a) Nano-differential scanning fluorimetry thermal melt analysis of GP2_{LCMV} (blue) and GP2_{LCMV}-I322F mutant (red). The first derivative of the ratio of fluorescence at 350 and 330 nm as a function of temperature is shown. This graph is a representative one from three independent repeats. (b) SYPRO orange thermo-fluorescence melt experiments of GP2_{LCMV} (blue) and GP2_{LCMV}-I322F mutant (red). The first derivative of the fluorescence as a function of temperature is shown. Each curve was derived from an independent repeat and is the average of several technical replicates. Peaks of local unfolding events that precede the global unfolding are pointed with blue and red arrows for GP2_{LCMV} and GP2_{LCMV}-I322F, respectively. (c) Nano-differential scanning fluorimetry thermal melt analysis of GP2_{LASV} (blue) and GP2_{LASV}-F316I mutant (red). The first derivative of the ratio of fluorescence at 350 and at 330 nm as a function of temperature is shown. This is a representative graph from three independent repeats. (d) SYPRO orange thermo-fluorescence melt experiments of GP2_{LASV} (blue) and GP2_{LASV}-F316I mutant (red). The first derivative of the fluorescence as a function of temperature is shown. Each curve was derived from an independent repeat and is the average of several technical replicates. Peaks of local unfolding events that precede the global unfolding are pointed with blue and red arrows for GP2_{LASV} and GP2_{LASV}-F316I, respectively. (e) Similarly to “d,” an SYPRO orange thermo-fluorescence melt experiments of GP2_{LASV} (blue) and GP2_{LASV}-R314A mutant (red).

normalized entry levels by the amounts of processed GP2 as indicated by the WB analyses (Fig. 4d), and further normalized cell entry by the amounts of pseudotyped viruses as we determined using RT-qPCR (Fig. 4g and h). Similarly to the effect on cell

fusion (Fig. 4b), F316I mutation in GPC_{LASV} reduced cell entry levels compared to GPC_{LASV}-WT (Fig. 4g). Remarkably, I322F mutation in GPC_{LCMV} increased cell entry levels compared to GPC_{LCMV}-WT (Fig. 4f), which is consistent with cell fusion

levels of these proteins (Fig. 4f). Thus, the packing quality of the hydrophobic core formed by the C helices at the post-fusion conformation of GP2 is an important determinant for the membrane fusion efficiency.

The effect of packing on GP2 thermostability

The energy that drives membrane fusion is ultimately donated by the change in free energy of the GPC spike complex upon transitioning from the metastable native pre-fusion conformation to the post-fusion state. Theoretically, for measuring such a change in free energy and evaluating any putative effect of mutagenesis, one first needs to obtain both the pre-fusion native spike and the post-fusion GP2 purified with their transmembrane domains. Technically, however, we do not currently have such capability. We thus decided to probe the thermostability of GP2 to gain insights about the effect of perturbing GP2_{LASV} and GP2_{LCMV} by mutating Phe316 and Ile322, respectively. We first used nano-differential scanning fluorimetry (nano-DSF), which follows the ratio of tryptophan fluorescence at 350 nm and 330 nm to monitor thermal unfolding of the GP2s. Both GP2_{LASV} and GP2_{LCMV} have two tryptophan residues each (positions 370 and 386 according to GP2_{LASV} numbering, Fig. 1c). Of these two positions, the tryptophan residues at the first position are located at the T helices and are exposed to solvent, hence not expected to provide a readable signal during thermal unfolding. The tryptophan residues at the second position are at the membrane-distal tips of the GP2s and are forming part of the hydrophobic cores. Examining the first derivatives for the thermal unfolding of GP2_{LCMV} and GP2_{LCMV}-I322F reveals single peaks that correspond to single global unfolding events (Fig. 5a). Both GP2_{LCMV} and GP2_{LCMV}-I322F exhibit similar T_m values of about 75 °C.

Since the only tryptophan residue that provides a fluorescence-change signal upon unfolding in this experiment is the buried tryptophan at the tip of the GP2, it can only indicate about the global unfolding and not about putative local unfolding events that may include the C helices. We therefore monitored the change of fluorescence of SYPRO-Orange during the thermal unfolding of the GP2s. SYPRO-Orange is a hydrophobic fluorescence dye that changes fluorescence when interacts with hydrophobic moieties of proteins and can thus reveal local unfolding events. Indeed, monitoring the unfolding of GP2_{LCMV} provides a complex unfolding curve that exhibits a distinct transition that precedes the global unfolding event (Fig. 5b). As expected, the global unfolding is observed at a lower temperature compared to the nano-DSF measurement as the interaction with SYPRO-Orange stabilizes the unfolded state.

Interestingly, repeating this experiment using GP2_{LCMV}-I322F indicates that similarly to the nano-DSF measurement the global unfolding occurs at the same temperature as in GP2_{LCMV} (Fig. 5b). However, there is an apparent shift in the transition that precedes the global unfolding, which occurs at a higher temperature in GP2_{LCMV}-I322F compared to GP2_{LCMV} (Fig. 5b). This observation implies that I322F mutation in LCMV increases the local stability of the membrane-proximal region of GP2_{LCMV}.

We next measured the thermostability of GP2_{LASV} and compared it to the thermostability of GP2_{LASV}-F316I. We first used nano-DSF to evaluate the global thermostability of the proteins (Fig. 5c). Surprisingly, GP2_{LASV}-F316I appears to be more stable compared to GP2_{LASV} with T_m of ~80 °C compared to ~74 °C for both proteins, respectively (Fig. 5c). Such increased global thermal stability is also evident following the fluorescence change of SYPRO-Orange (Fig. 5d). Interestingly, the unfolding of GP2_{LASV} also exhibits a local transition that precedes the global unfolding, similarly to GP2_{LCMV}. Unlike the global unfolding though, this local unfolding occurs at the same temperature in both GP2_{LASV} and GP2_{LASV}-F316I (Fig. 5d). Thus, introducing the F316I mutation to GP2_{LASV} stabilizes the global structure but most likely not through stabilizing the interaction of the C helices at the membrane-proximal region.

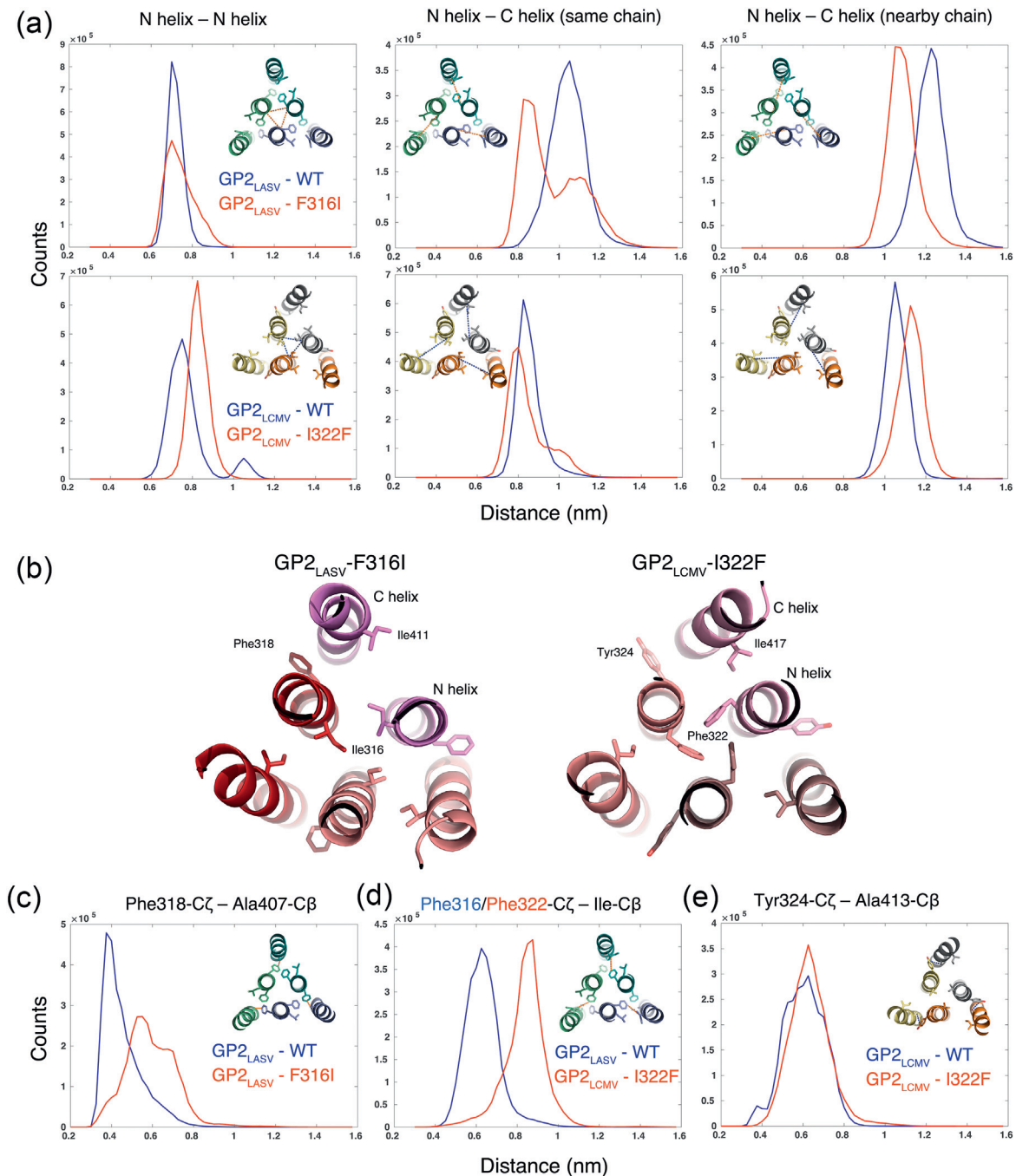
Observing this complex effect of the F316I mutation prompted us to test additional mutation. Arg314 GP2_{LASV} forms a salt-bridge that stabilizes the interaction between the C and N helices (Fig. 2b). We produced a GP2_{LASV}-R314A variant and tested its thermostability using SYPRO-Orange (Fig. 5e). The melting profile of GP2_{LASV}-R314A indicates a reduced global thermostability with an evident change of the local transition as well (Fig. 5e). These changes in thermostability could be rationalized by the loss of the salt-bridge. Observing these shifts in the local and global transitions in the case of GP2_{LASV}-R314A further implies that the complex profile obtained for GP2_{LASV}-F316I (Fig. 5d) may result from some unpredicted rearrangements of core residues following mutagenesis.

Organization of the cores following mutagenesis

To better understand how the hydrophobic-core mutations affect the stability of the GP2 modules and consequently the overall activity of the GPC spike complexes, we performed molecular dynamics (MD) simulations for GP2_{LASV}, GP2_{LASV}-F316I, GP2_{LCMV}, and GP2_{LCMV}-I322F. The conformational dynamics of each system were studied by four MD simulations, each of 250 ns. We aggregated the sampled conformations from the four independent runs and followed some representative pairwise distances that may highlight the effect of the mutations on the

structure. We plotted the pairwise distance distributions between the inner N helices, and the distances between the C helices to the two adjacent N helices (Fig. 6a). Interestingly, in the MD simulations, Ile316 of GP2_{LASV}-F316I arranges at the interface between the three N helices (Fig. 6b) in a similar fashion to that of Ile322 in the crystal structure of GP2_{LCMV} (Fig. 3d). As a consequence, Phe318 that mostly interacts with Phe316 and Ala407 in GP2_{LASV}-WT (narrow distance distribution of ~0.4 nm for Phe318-C ζ and Ala407-C β , Fig. 6c), is fluctuating between a similar

state and a state in which it points away from the core underneath the C helix (Fig. 6b, c). The outward configuration of Phe318 is similar to Tyr324 as seen in the crystal structure of GP2_{LCMV} (Fig. 3d). This outward configuration reduces the extent of hydrophobic interactions between the C and N helices and allows the C helices to move closer toward the N helices compared to GP2_{LASV}-WT (Fig. 6a). Interestingly, whereas the distance of the C helix to the N helix of the adjacent chain seems to follow a single normal distribution, the distance between the C helix



to the N helix from the same chain fluctuates and adopts a wider two-state distribution in GP2_{LASV}-F316I (Fig. 6a). Such a longer distance state is similar in length to the distribution observed in GP2_{LASV}-WT (Fig. 6a), and it might be needed to accommodate Phe318.

In GP2_{LCMV}-I322F, the MD simulations reveal that Phe322 is pointing to the inner space between the N helices (Fig. 6b), forming hydrophobic interactions around the symmetry axis of the trimer. Due to the larger side-chain of the phenylalanine compared to isoleucine, the N helices in GP2_{LCMV}-I322F slightly move apart from each other (Fig. 6a). Noteworthy, during the simulations, Phe322 also samples a rotamer that brings its side-chain to a close proximity with Ile417 (i.e., 0.8 nm or less for Phe322-C ζ and Ile417-C β) that is on the C helix (Fig. 6d), which in turn samples a longer distance to the same-chain N helix to make room for the Phe322 side-chain (Fig. 6a). Although transient, this Phe322-Ile417 interaction contributes to stabilizing the C helix. The main reason for the transient nature of this interaction is the inability of Tyr324 of GP2_{LCMV} to stabilize this hydrophobic core as Phe318 of GP2_{LASV} does (Fig. 3d).

LASV has more efficient fusion machinery compared to LCMV

Following our observations that GP2_{LASV} forms a more elaborated set of hydrophobic interactions between its C and N helices compared to GP2_{LCMV}, we further compared the fusogenic potential of the GPCs derived from these two viruses. GPC_{LASV} and GPC_{LCMV} are expressed and processed to overall similar levels in HEK293 cells as indicated by WB analysis (Fig. 7a). In side-by-side comparisons using

syncytia formation assay, the GPC_{LASV} seems to be a better fusogen compared to GPC_{LCMV} (Fig. 7b). Furthermore, pseudotyped viruses bearing the GPC_{LASV} are more efficient in cell entry compared to ones that bear GPC_{LCMV} (Fig. 7c). Thus, GPC_{LASV} makes a more efficient fusogen compared to GPC_{LCMV}.

Discussion

LASV is the most virulent of the Old World mammarenaviruses. In this study, we investigated the post-fusion state of its GP2 module (Fig. 1b). We found that GP2_{LASV} adopts a canonical post-fusion structure that is similar to the determined structures of GP2_{LCMV} [40] and of GP2_{GTOV} [41] (Figs. 1b and 2a), despite a previous observation by electron microscopy that suggested otherwise [39]. Structural analysis indicated some differences between GP2_{LASV} and the other GP2 from mammarenaviruses for which structural data are available. Specifically, the packing of the C helices against the N helices that make together the most membrane-proximal region of GP2 differs in the available models (Fig. 2b). Compared to GP2_{LCMV}, GP2_{LASV} forms more hydrophobic interactions between its C helices and its N helices (Fig. 3b), minimizing the formation of energetically unfavored hydrophobic cavities in this region (Fig. 3a). The change in free energy that is associated with the transition from the pre-fusion native state of the complete spike complex to the post-fusion state of its GP2 is ultimately driving membrane fusion. While the global collapse of the extended intermediate into the helical bundle configuration is needed to bring the viral and the host membranes into close proximity, we speculate that the interaction of the C helices with the N helices,

Fig. 6. MD simulations reveal the structural rearrangements following mutagenesis. (a) Accumulated pairwise distances between the helices. The distributions of distances were calculated from aggregating the four different simulations for each protein and measuring the three relevant distances in each time-step. In each image, the measured distances are indicated with dashed lines. The upper panel of images shows distance distributions for GP2_{LASV}-WT and GP2_{LASV}-F316I in blue and red, respectively. The lower panel of images shows distance distributions for GP2_{LCMV}-WT, and GP2_{LCMV}-I322F in blue and red, respectively. The N helix to N helix distances were calculated between the C α atoms of residue 316 for GP2_{LASV} and between C α atoms of residue 322 for GP2_{LCMV}. The N helix to C helix distances were calculated between C α atoms of residue 316 to the C α atom of Ile411 in the case of GP2_{LASV} and between C α atoms of residue 322 and C α atom of Ile417 in the case of GP2_{LCMV}. These distances were calculated both for pairs that are on the same chain as well as for pairs that are located on two nearby chains. (b) Snapshot from the MD simulations. Two snapshots that were taken from the MD simulations of GP2_{LASV}-F316I (left) and GP2_{LCMV}-I322F (right) are shown and illustrate common configurations of the core residues. (c) Rotameric configuration of Phe318 of GP2_{LASV}. Distance distributions between C ζ atom of Phe318 and C β atom of Ala407 in GP2_{LASV}-WT and GP2_{LASV}-F316I in blue and red, respectively. Short distances (~0.4 nm) indicate that Phe318 points toward the hydrophobic core underneath the C helix, and long distances (~0.6 nm) indicate that Phe318 points outward. (d) Rotameric configuration of Phe316/Phe322 of GP2_{LASV} and GP2_{LCMV}-I322F, respectively. Distance distributions between C ζ atoms of the phenylalanine residues and C β atom of Ile411 for GP2_{LASV} (blue) or Ile417 for GP2_{LCMV}-I322F (red) are indicated. Short distances (below 0.8 nm) indicate that the phenylalanine interacts with the isoleucine, and larger distances (above 0.8 nm) indicate that the phenylalanine points toward the central region between the N helices. (e) Rotameric configuration of Tyr324 of GP2_{LCMV}. Distance distributions between C ζ atom of Tyr324 and C β atom of Ala413 in GP2_{LCMV}-WT and GP2_{LCMV}-I322F in blue and red, respectively. Distances of about 0.6 nm indicate that Tyr324 points outward from the hydrophobic core.

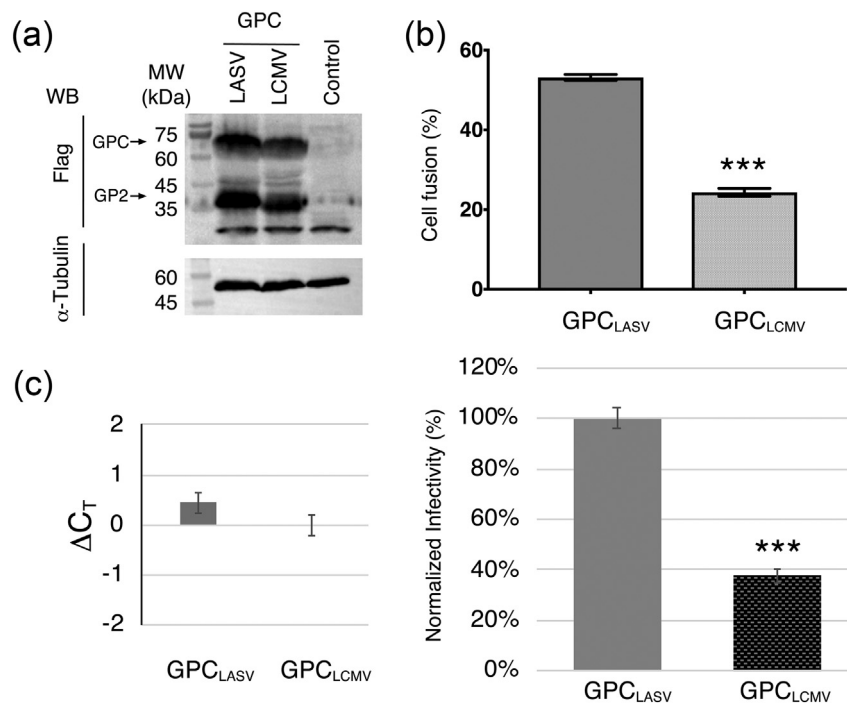


Fig. 7. The spike complex of LASV is more efficient than of LCMV in driving cell entry. (a) Expression and processing profiles of GPC_{LASV} compared to GPC_{LCMV}. Western blot analyses show Flag-GPC constructs that were transiently transfected into HEK293 cells. Unprocessed GPCs as well as the GP2 portion after cleavage are indicated with black arrows. Detecting α -tubulin was used as a loading control. This image is a representative one out of two independent repeats. (b) Membrane fusion activities measured by syncytia formation assays at pH 4.0. The level of activity for both GPC_{LASV} and GPC_{LCMV} was evaluated in multiple independent experiments. The fusion efficiency of GPC_{LCMV} is significantly ($p < 0.001$, two-sided Student's *t*-test) lowered compared with GPC_{LASV}. (c) Cell entry levels of MLV-based pseudotyped viruses bearing GPC spike complexes from LASV and LCMV. Amount of pseudotyped viruses were determined using RT-qPCR and used to normalize infectivity data. Cell entry levels were measured by luciferase activity. This assay was repeated three independent times. The difference in cell entry is statistically significant ($p < 0.001$, two-sided Student's *t*-test).

which most likely represents the last “zipping” step of the GP2 fusogen, would be specifically important for promoting the fusion pore formation and for stabilizing it before expansion. Our data support this hypothesis as reducing the interaction strength by introducing a F316I mutation to GPC_{LASV} reduces its membrane fusion and cell entry activities (Fig. 4b and g). More strikingly, increasing the interaction between these helices by introducing an I322F mutation to GPC_{LCMV} augmented its fusogenic activity (Fig. 4f) and promoted more efficient cell entry (Fig. 4h).

Thermostability measurements of the GP2 variants indicated that in the case of GP2_{LCMV}, introducing the I322F mutation did not affect the global melting temperature (Fig. 5a) but did increase the temperature of the observed local rearrangement that precedes global unfolding (Fig. 5b). The MD simulations indicated that Phe322 in GP2_{LCMV} maintains strong hydrophobic core near the 3-fold symmetry axis (Fig. 6b) like Ile322 (Fig. 3d), probably contributing for the global thermostability. In addition, Phe322 in GP2_{LCMV} also contributes to

the interaction with the C helix by pointing toward Ile417 (Fig. 6d) in a fraction of the time. These interactions that only form in the mutated GP2_{LCMV} provide an explanation for local thermostability gain (Fig. 5b) and rationalize the augmented fusogenic potential of the mutated GPC_{LCMV} (Fig. 4f and h).

Considering GP2_{LASV}, the surprising increase in the global thermostability of GP2_{LASV} upon introducing the F316I mutation is rationalized by the formation of a tightly packed hydrophobic interactions between the N helices by the three Ile316, as indicated by the MD simulations (Fig. 6b), which is lacking in the unmutated GP2_{LASV}. This observation suggests that a major determinant for the global stability of GP2 is the strength of interactions between the central helices. Interestingly, the F316I mutation in GP2_{LASV} that negatively affected the fusogenic activity of GPC_{LASV} did not seem to lower the temperature for the first local transition, as might have been expected. An explanation for that could be that nearby residues, like Phe318, (Fig. 3b) that helps to form tighter packing in this region of GP2_{LASV} are able to maintain some interactions with

the C helix and prevent changes in the temperature of unfolding for this local region. The MD simulations support this idea as Phe318 of GP2_{LASV} is frequently shuttling between the outward and inward configurations (Fig. 6c). Nevertheless, the strength of interactions between the C and N helices in GP2_{LASV}-F316I is reduced, which ultimately affects the function of GPC_{LASV}-F316I (Fig. 4b and g).

Our structural and biochemical data suggest that the extent of stabilizing interactions that the C helices make with the N helices at the post-fusion state of GP2 affects the fusogenic potential of the spike complex. In a side-by-side comparison, the GPC_{LASV} is more efficient than GPC_{LCMV} in promoting membrane fusion (Fig. 7b) as well as cell entry of pseudotyped viruses (Fig. 7c). While more efficient GPC_{LASV}-mediated cell entry could be partially explained by the unique mechanism of LASV [36] that binds LAMP1 [34] as a way to coordinate spike triggering for efficient cell entry [35], the more efficient cell fusion activity is likely influenced by *bona fide* differences in the fusogenic abilities of the two proteins. A better fusogenic potential would be a beneficial property for viruses as it increases their chances to penetrate their target cells successfully. The differences in the packing quality of the C helices that our current study revealed, makes up one of the factors that allow GPC_{LASV} to fuse membranes more efficiently compared to GPC_{LCMV} and ultimately contributes to the higher virulence of LASV compared to some of the other viruses of this family.

Materials and Methods

Vector construction and baculovirus production

Codon-optimized synthetic genes (GenScript) encoding for GPC_{LASV} (Josiah) and GPC_{LCMV} (Armstrong) were served as templates for PCR to generate GP2_{LASV} and GP2_{LCMV} that were sub-cloned into the pACgp67b expression vector (BD Biosynthesis) to include an N-terminal 6XHis tag followed by TEV protease cleavage site. For high-level expression, baculoviruses were produced by co-transfecting sf9 cells with 0.3 µg of GP2_{LASV}-pACgp67b or GP2_{LCMV}-pACgp67b and 0.25 µg of linearized baculovirus genome (AB-vector) using Escort-IV transfection reagent (Sigma). Four days later, media with viral particles were collected (P0), and viral titers were amplified by infecting fresh cells growing in suspension for 7 days (P1, P2). Subsequently, media with amplified viruses were collected.

Protein expression and purification

Two liters of Tni cells at 1 M cells/mL in ESF-921 medium (Expression Systems) was infected with

amplified viruses. Supernatants containing the secreted protein were collected after 3 days, were supplemented with 0.02% (w/v) sodium azide, 100 µM phenylmethylsulfonyl fluoride, and 40 mM Tris (pH -8), and were subsequently buffer exchanged to TBS [20 mM Tris (pH 8.0), 150 mM sodium chloride and 0.02% (w/v) sodium azide]. Protein was captured from media using HiTrap IMAC FF Ni²⁺ affinity column (GE Healthcare) and further purified using Superdex200 10/300 size exclusion chromatography (GE Healthcare). Protein was then cleaved by TEV protease overnight at 30 °C in TBS. Subsequently, the cleaved protein was isolated using Superdex200 10/300 size exclusion chromatography (GE Healthcare). For crystallization experiments, the protein was concentrated to 11 mg/mL in TBS using an Amicon concentration (Millipore).

Crystallization

Protein was crystallized using hanging-drop vapor diffusion method. Initial crystallization conditions were identified in sitting-drop vapor diffusion crystallization experiments set by a Mosquito crystallization robot (TTP Labs). For crystallization experiments, we used sets of 60, 120, and 180 nL drops of protein mixed with 120 nL reservoirs of commercially available crystallization screens. Initial crystallization hits appeared at 20 °C using PEGRx HT (Hampton) screen and were then manually optimized. Crystals suitable for x-ray data collection were obtained after mixing a protein with well solution in a ratio of 1:1 with 100 mM Bis-Tris (pH -6.5), 500 mM sodium potassium tartrate tetrahydrate, 6.0% (w/v) PEG 10000, 15 mM HCl, and 3% (w/v) diamino-pentane-dihydrochloride.

Data collection, structure solution, and refinement

X-ray diffraction data were collected at the European Synchrotron Radiation Facility beamline ID29 using a PILATUS 6 M detector. Diffraction data were collected from crystals at 100 °K. Diffraction data were indexed and integrated using XDS [45] and scaled using Aimless [46]. Molecular replacement solution was found using Phaser [47]. Model building and refinement were done in an iterative fashion using Coot [48] and Phenix [49], respectively. For structure validation, we used MolProbity [50].

Cell-cell fusion assay

HEK293T cells were seeded (~150,000 cells/well) in a 24-well plate pre-coated with poly-L-lysine (Sigma). Cells were transfected 24 h later with 0.4 µg DNA of the indicated GPC constructs using polyethyleneimine 40,000 Da (Polysciences). Twenty-four hours later, cells were rinsed once

with growing media supplemented with 20 mM MES and titrated to pH 4.0 or 4.5, and were incubated with the same media for 10 min before washing and incubation with regular HEK293T media for 2 h at 37 °C for recovery. Afterward, cells were fixed in 3.7% (v/v) formaldehyde solution (J.T. Baker) in phosphate-buffered saline (Biological Industries) for 10 min. Phase images of syncytia were taken at $\times 10$ magnification using a phase microscope, and their boundaries were automatically selected using the versatile wand tool of ImageJ [51]. Activity is expressed as percent of the syncytia area in the total area of the field of view.

Pseudotyped viruses production and cell entry assays

MLV-based pseudo-typed viruses that deliver luciferase reporter gene when enter cells were produced by transfecting retroviral transfer vector pLXIN-Luc (pLXIN-Luc was a gift from Alice Wong—Addgene plasmid no. 60683) along with pcDNA plasmids encoding the envelope GPC_{LASV} or GPC_{LCMV} into the GP2-293 Retroviral packaging cell line (Clontech). Media containing pseudotyped viruses were collected 48 post-transfection. Viral containing media were subsequently supplemented with PEG 6000 (Sigma) in phosphate-buffered saline to a final concentration of 8% (w/v) and incubated for 18 h at 4 °C. Viruses were then pelleted by centrifugation at 10,000g for 20 min. Pellets of viruses were resuspended in cell media. To test cell entry potential of the GPCs, we seeded 30,000 HEK293T cells on poly-L-lysine pre-coated white, chimney 96-well plates (Greiner Bio-One). Cells were left to adhere for 24 h, followed by the addition of 50 μ L of concentrated pseudotyped viruses. Cells were washed from viruses at 18 h post-infection, and luminescence from the activity of luciferase was measured at 48 h post-infection using a TECAN plate reader (LabX) after applying 100 μ L Bright-Glo reagent (Promega) on cells. For comparing infectivity, the reads were normalized by the amount of processed GPC as determined by densitometry analysis (ImageJ [51]) of the GP2 bands.

RT-qPCR quantification of pseudotyped viruses

To quantify pseudotyped viruses, we used RT-qPCR for determining the RNA levels of the Luciferase reporter gene. Media containing virus like particles was centrifuged at 13,000 rpm 4 °C for 10 min, and 50 μ L from the supernatant was treated with 2 μ g/ml RNase A (Bio Basic Inc) for 10 min at RT. To inhibit RNase A activity, 40 units of RNase inhibitor murine (NEB) were added and reaction was incubated for 10 min at 37 °C. RNA was then prepared from treated media using RNAeasy mini kit (Qiagen). To eliminate remnants of the

Luciferase-containing retroviral vectors, RNA was treated with RNase-free DNase (NEB) for 10 min at 37 °C, followed by heat inactivation in 75 °C for 10 min. Thereafter, cDNA was prepared from RNA using high-capacity cDNA reverse transcription kit (Applied Biosystems). cDNA was then diluted 1:40 and subjected to quantitative PCR (qPCR) using specific primers for Luciferase, and Fast SYBR green master mix (Applied Biosystems).

α -DG pull-down assay

HEK293T cells were transfected with Flag-tagged GPC_{LASV}, GPC_{LCMV} and their mutant variants. At 48 h post-transfection, cells were lysed with Triton buffer [50 mM Tris-HCl (pH 8.0), 150 mM sodium chloride, 1 mM EDTA, 0.5% (v/v) Triton]. Lysates were clarified by centrifugation, and supernatants were incubated with EZview Red anti-Flag beads (Sigma-Aldrich). Beads were then washed and incubated with whole-cell lysates of non-transfected cells prepared in NET1 buffer [50 mM Tris-HCl (pH 8.0), 150 mM sodium chloride, 1 mM EDTA, 0.5% (v/v) octylphenoxypolyethoxyethanol (IGEPAL; Sigma)]. Beads were washed, and proteins were eluted using a 3 \times Flag peptide (Sigma-Aldrich). Eluents were boiled in sample buffer and subjected to SDS-PAGE and immunoblotting using anti- α -DG. As a control GPC_{LASV}, GPC_{LCMV} and their mutant derivatives expression levels were examined. Lysates were further subjected to Western blot analyses using anti FLAG (Thermo Fisher) and anti- α -tubulin antibodies, clone DM1A (Millipore) for expression and load controls.

SYPRO-Orange fluorescence melt assay

Protein melt experiments were performed using a StepOne Real-Time PCR System (Thermo Fisher) in a 96-well format by monitoring the change in fluorescence of SYPRO® Orange (Sigma). Protein aliquots in thin-wall (low-profile) PCR plates (Axygen) at 12.5 μ g/well in the presence of 90X SYPRO® Orange protein gel stain solution (Sigma) in an acidic buffer [20 mM sodium citrate (pH -5), 150 mM NaCl, 2% (v/v) dimethyl sulfoxide, 0.02% (w/v) sodium azide] at final volumes of 25 μ L were analyzed. Plates were sealed using Platemax® UltraClear sealing film (Axygen). A linear gradient of temperature ranging from 25 to 90 °C was used for the melt experiments. The temperature was ramped at a rate of 0.2 °C/min.

Nano-differential scanning fluorimetry

To determine the T_m of GP2_{LASV}, GP2_{LCMV}, and their mutant variants, a label-free nDSF was utilized. To measure the melting temperatures, 10 μ L of each GP2 at 0.9 mg/mL was aspirated into the glass capillary tubes and analyzed at a scan rate of 0.5 °C/

min from 25 °C to 90 °C. The software analyzed the thermal denaturation curve and determined the onset and melting temperatures of each protein.

MD simulations

The conformational stability of GP2_{LASV} and GP2_{LCMV} as well as their mutants was studied by MD simulations carried out using GROMACS 2019.0 [52] with the AMBER99SB-ILDN force-field [53]. All models were solvated with water molecules (TIP3P), and sodium and chloride ions were added to achieve a concentration of 0.125 M, with adjustments to neutralize the system. The solvated models were energy minimized and followed by PT and NPT equilibration runs of 100 ps each. To allow a smaller simulation box, two CA atoms in the upper helices of each chain (Ile334 and His354 in GP2_{LASV}, Leu340, and His360 in GP2_{LCMV}) were positionally restrained to avoid tumbling of the trimer. For each model, four MD runs of 250 ns each were performed. All distance measurement histograms in each model are combined from the four runs. Missing residues in GP2_{LASV} and GP2_{LCMV} at the head domains were modeled using SWISS-MODEL [54], and point mutations were modeled using Coot [48].

Data availability

The coordinate file and structure factors are available at the Protein Data Bank under accession number 5OMI.

Acknowledgments

Diffraction experiments were performed at beamline ID29 at the European Synchrotron Radiation Facility, Grenoble, France. We are grateful to Antoine Royant at the European Synchrotron Radiation Facility for providing assistance in using beamline ID29 and to Linda Shimon for her assistance in data collection.

Ron Diskin is the incumbent of the Tauro career development chair in biomedical research. This research was supported by a research grant from the Enoch Foundation, a research grant from the Abramson Family Center for Young Scientists, a research grant from Ms. Rudolfine Steindling, and by the I-CORE Program of the Planning and Budgeting Committee and The Israel Science Foundation (Grant No. 1775/12)

Received 6 December 2018;

Received in revised form 8 April 2019;

Accepted 8 April 2019

Available online 18 April 2019

Keywords:
viral proteins;
crystal structure;
membrane fusion;
cell entry;
virulence

Abbreviations used:

LASV, Lassa virus; GPC, glycoprotein precursor; GP1 and GP2, glycoproteins 1 and 2; LAMP1, lysosomal-associated membrane protein 1; MD, molecular dynamics; TEV, tobacco etch virus.

References

- [1] S.R. Radoshitzky, Y. Bao, M.J. Buchmeier, R.N. Charrel, A.N. Clawson, C.S. Clegg, et al., Past, present, and future of arenavirus taxonomy, *Arch. Virol.* 160 (2015) 1851–1874.
- [2] M.B. Oldstone, Arenaviruses. I. The epidemiology molecular and cell biology of arenaviruses. Introduction, *Curr. Top. Microbiol. Immunol.* 262 (2002) V–XII.
- [3] M.B. Oldstone, Arenaviruses. II. The molecular pathogenesis of arenavirus infections. Introduction, *Curr. Top. Microbiol. Immunol.* 263 (2002) V–XII.
- [4] T.W. Geisbert, P.B. Jahrling, Exotic emerging viral diseases: progress and challenges, *Nat. Med.* 10 (2004) S110–S121.
- [5] M.L. Moraz, S. Kunz, Pathogenesis of arenavirus hemorrhagic fevers, *Expert Rev. Anti-Infect. Ther.* 9 (2011) 49–59.
- [6] J.K. Richmond, D.J. Baglolle, Lassa fever: epidemiology, clinical features, and social consequences, *BMJ.* 327 (2003) 1271–1275.
- [7] J.B. McCormick, S.P. Fisher-Hoch, Lassa fever, *Curr. Top. Microbiol. Immunol.* 262 (2002) 75–109.
- [8] S. Kunz, P. Borrow, M.B. Oldstone, Receptor structure, binding, and cell entry of arenaviruses, *Curr. Top. Microbiol. Immunol.* 262 (2002) 111–137.
- [9] J.M. Rojek, S. Kunz, Cell entry by human pathogenic arenaviruses, *Cell. Microbiol.* 10 (2008) 828–835.
- [10] D.J. Burri, J.R. da Palma, S. Kunz, A. Pasquato, Envelope glycoprotein of arenaviruses, *Viruses.* 4 (2012) 2162–2181.
- [11] J.H. Nunberg, J. York, The curious case of arenavirus entry, and its inhibition, *Viruses.* 4 (2012) 83–101.
- [12] B. Eschli, K. Quirin, A. Wept, J. Weber, R. Zinkernagel, H. Hengartner, Identification of an N-terminal trimeric coiled-coil core within arenavirus glycoprotein 2 permits assignment to class I viral fusion proteins, *J. Virol.* 80 (2006) 5897–5907.
- [13] W.R. Beyer, D. Popplau, W. Garten, D. von Laer, O. Lenz, Endoproteolytic processing of the lymphocytic choriomeningitis virus glycoprotein by the subtilase SKI-1/S1P, *J. Virol.* 77 (2003) 2866–2872.
- [14] O. Lenz, J. ter Meulen, H.D. Klenk, N.G. Seidah, W. Garten, The Lassa virus glycoprotein precursor GP-C is proteolytically processed by subtilase SKI-1/S1P, *Proc. Natl. Acad. Sci. U. S. A.* 98 (2001) 12701–12705.
- [15] J.M. Rojek, A.M. Lee, N. Nguyen, C.F. Spiropoulou, S. Kunz, Site 1 protease is required for proteolytic processing of the glycoproteins of the South American hemorrhagic fever

- viruses Junin, Machupo, and Guanarito, *J. Virol.* 82 (2008) 6045–6051.
- [16] D.J. Burri, G. Pasqual, C. Rochat, N.G. Seidah, A. Pasquato, S. Kunz, Molecular characterization of the processing of arenavirus envelope glycoprotein precursors by subtilisin kexin isozyme-1/site-1 protease, *J. Virol.* 86 (2012) 4935–4946.
- [17] H. Cohen-Dvashi, I. Kilimnik, R. Diskin, Structural Basis for Receptor Recognition by Lujo Virus, *bioRxiv*, 2018.
- [18] J. Abraham, K.D. Corbett, M. Farzan, H. Choe, S.C. Harrison, Structural basis for receptor recognition by New World hemorrhagic fever arenaviruses, *Nat. Struct. Mol. Biol.* 17 (2010) 438–444.
- [19] S.C. Harrison, Viral membrane fusion, *Nat. Struct. Mol. Biol.* 15 (2008) 690–698.
- [20] G. Pasqual, J.M. Rojek, M. Masin, J.Y. Chatton, S. Kunz, Old world arenaviruses enter the host cell via the multivesicular body and depend on the endosomal sorting complex required for transport, *PLoS Pathog.* 7 (2011), e1002232.
- [21] S.R. Radoshitzky, J. Abraham, C.F. Spiropoulou, J.H. Kuhn, D. Nguyen, W. Li, et al., Transferrin receptor 1 is a cellular receptor for New World haemorrhagic fever arenaviruses, *Nature.* 446 (2007) 92–96.
- [22] S.R. Radoshitzky, J.H. Kuhn, C.F. Spiropoulou, C.G. Albarino, D.P. Nguyen, J. Salazar-Bravo, et al., Receptor determinants of zoonotic transmission of New World hemorrhagic fever arenaviruses, *Proc. Natl. Acad. Sci. U. S. A.* 105 (2008) 2664–2669.
- [23] J. Abraham, J.A. Kwong, C.G. Albarino, J.G. Lu, S.R. Radoshitzky, J. Salazar-Bravo, et al., Host-species transferrin receptor 1 orthologs are cellular receptors for nonpathogenic new world clade B arenaviruses, *PLoS Pathog.* 5 (2009), e1000358.
- [24] H. Choe, S. Jemielity, J. Abraham, S.R. Radoshitzky, M. Farzan, Transferrin receptor 1 in the zoonosis and pathogenesis of New World hemorrhagic fever arenaviruses, *Curr. Opin. Microbiol.* 14 (2011) 476–482.
- [25] S.R. Radoshitzky, L.E. Longobardi, J.H. Kuhn, C. Retterer, L. Dong, J.C. Clester, et al., Machupo virus glycoprotein determinants for human transferrin receptor 1 binding and cell entry, *PLoS One* 6 (2011), e21398.
- [26] M. Zong, I. Fofana, H. Choe, Human and host species transferrin receptor 1 use by North American arenaviruses, *J. Virol.* 88 (2014) 9418–9428.
- [27] W. Cao, M.D. Henry, P. Borrow, H. Yamada, J.H. Elder, E.V. Ravkov, et al., Identification of alpha-dystroglycan as a receptor for lymphocytic choriomeningitis virus and Lassa fever virus, *Science.* 282 (1998) 2079–2081.
- [28] C.F. Spiropoulou, S. Kunz, P.E. Rollin, K.P. Campbell, M.B. Oldstone, New World arenavirus clade C, but not clade A and B viruses, utilizes alpha-dystroglycan as its major receptor, *J. Virol.* 76 (2002) 5140–5146.
- [29] S. Kunz, J.M. Rojek, M. Kanagawa, C.F. Spiropoulou, R. Barresi, K.P. Campbell, et al., Posttranslational modification of alpha-dystroglycan, the cellular receptor for arenaviruses, by the glycosyltransferase LARGE is critical for virus binding, *J. Virol.* 79 (2005) 14282–14296.
- [30] S. Kunz, J.M. Rojek, M. Perez, C.F. Spiropoulou, M.B. Oldstone, Characterization of the interaction of Lassa fever virus with its cellular receptor alpha-dystroglycan, *J. Virol.* 79 (2005) 5979–5987.
- [31] M. Shimojima, U. Stroher, H. Ebihara, H. Feldmann, Y. Kawaoka, Identification of cell surface molecules involved in dystroglycan-independent Lassa virus cell entry, *J. Virol.* 86 (2012) 2067–2078.
- [32] C. Fedeli, G. Torriani, C. Galan-Navarro, M.L. Moraz, H. Moreno, G. Gerold, et al., Axl can serve as entry factor for Lassa virus depending on the functional glycosylation of dystroglycan, *J. Virol.* 92 (2018).
- [33] M. Raaben, L.T. Jae, A.S. Herbert, A.I. Kuehne, S.H. Stubbs, Y.Y. Chou, et al., NRP2 and CD63 are host factors for Lujo virus cell entry, *Cell Host Microbe* 22 (2017) 688–696 (e5).
- [34] L.T. Jae, M. Raaben, A.S. Herbert, A.I. Kuehne, A.S. Wirchnianski, T.K. Soh, et al., Virus entry. Lassa virus entry requires a trigger-induced receptor switch, *Science.* 344 (2014) 1506–1510.
- [35] H. Cohen-Dvashi, H. Israeli, O. Shani, A. Katz, R. Diskin, Role of LAMP1 binding and pH sensing by the spike complex of Lassa virus, *J. Virol.* 90 (2016) 10329–10338.
- [36] H. Israeli, H. Cohen-Dvashi, A. Shulman, A. Shimon, R. Diskin, Mapping of the Lassa virus LAMP1 binding site reveals unique determinants not shared by other old world arenaviruses, *PLoS Pathog.* 13 (2017), e1006337.
- [37] H. Cohen-Dvashi, N. Cohen, H. Israeli, R. Diskin, Molecular mechanism for LAMP1 recognition by Lassa virus, *J. Virol.* 89 (2015) 7584–7592.
- [38] K.M. Hastie, M.A. Zandonatti, L.M. Kleinfelter, M.L. Heinrich, M.M. Rowland, K. Chandran, et al., Structural basis for antibody-mediated neutralization of Lassa virus, *Science.* 356 (2017) 923–928.
- [39] S. Li, Z. Sun, R. Pryce, M.L. Parsy, S.K. Fehling, K. Schlie, et al., Acidic pH-induced conformations and LAMP1 binding of the Lassa virus glycoprotein spike, *PLoS Pathog.* 12 (2016), e1005418.
- [40] S. Igonet, M.C. Vaney, C. Vonrhein, G. Bricogne, E.A. Stura, H. Hengartner, et al., x-ray structure of the arenavirus glycoprotein GP2 in its postfusion hairpin conformation, *Proc. Natl. Acad. Sci. U. S. A.* 108 (2011) 19967–19972.
- [41] M.L. Parsy, K. Harlos, J.T. Huisken, T.A. Bowden, Crystal structure of Venezuelan hemorrhagic fever virus fusion glycoprotein reveals a class 1 postfusion architecture with extensive glycosylation, *J. Virol.* 87 (2013) 13070–13075.
- [42] L.V. Chernomordik, M.M. Kozlov, Mechanics of membrane fusion, *Nat. Struct. Mol. Biol.* 15 (2008) 675–683.
- [43] K.M. Hastie, S. Igonet, B.M. Sullivan, P. Legrand, M.A. Zandonatti, J.E. Robinson, et al., Crystal structure of the prefusion surface glycoprotein of the prototypic arenavirus LCMV, *Nat. Struct. Mol. Biol.* 23 (2016) 513–521.
- [44] X. Robert, P. Gouet, Deciphering key features in protein structures with the new ENDscript server, *Nucleic Acids Res.* 42 (2014) W320–W324.
- [45] W. Kabsch, Xds, *Acta Crystallogr. Sect. D Biol. Crystallogr.* 66 (2010) 125–132.
- [46] M.D. Winn, C.C. Ballard, K.D. Cowtan, E.J. Dodson, P. Emsley, P.R. Evans, et al., Overview of the CCP4 suite and current developments, *Acta Crystallogr. D Biol. Crystallogr.* 67 (2011) 235–242.
- [47] A.J. McCoy, R.W. Grosse-Kunstleve, P.D. Adams, M.D. Winn, L.C. Storoni, R.J. Read, Phaser crystallographic software, *J. Appl. Crystallogr.* 40 (2007) 658–674.
- [48] P. Emsley, B. Lohkamp, W.G. Scott, K. Cowtan, Features and development of Coot, *Acta Crystallogr. D Biol. Crystallogr.* 66 (2010) 486–501.
- [49] P.D. Adams, P.V. Afonine, G. Bunkoczi, V.B. Chen, I.W. Davis, N. Echols, et al., PHENIX: a comprehensive Python-based system for macromolecular structure solution, *Acta Crystallogr. D Biol. Crystallogr.* 66 (2010) 213–221.
- [50] V.B. Chen, W.B. Arendall III, J.J. Headd, D.A. Keedy, R.M. Immormino, G.J. Kapral, et al., MolProbity: all-atom structure

- validation for macromolecular crystallography, *Acta Crystallogr. Sect. D Biol. Crystallogr.* 66 (2010) 12–21.
- [51] C.A. Schneider, W.S. Rasband, K.W. Eliceiri, NIH Image to ImageJ: 25 years of image analysis, *Nat. Methods* 9 (2012) 671–675.
- [52] S. Pronk, S. Pall, R. Schulz, P. Larsson, P. Bjelkmar, R. Apostolov, et al., GROMACS 4.5: a high-throughput and highly parallel open source molecular simulation toolkit, *Bioinformatics*. 29 (2013) 845–854.
- [53] K. Lindorff-Larsen, S. Piana, K. Palmo, P. Maragakis, J.L. Klepeis, R.O. Dror, et al., Improved side-chain torsion potentials for the Amber ff99SB protein force field, *Proteins*. 78 (2010) 1950–1958.
- [54] T. Schwede, J. Kopp, N. Guex, M.C. Peitsch, SWISS-MODEL: an automated protein homology-modeling server, *Nucleic Acids Res.* 31 (2003) 3381–3385.